


Long-range and local structure evolution of $Y_{1.8}Eu_{0.2}Ge_2O_7$ under static high pressuresRahul Kaiwart^{1,3}, Abhilash Dwivedi¹, M. Modak¹, Adish Tyagi^{2,3}, Sandeep Nigam^{2,3}, K. K. Pandey^{1,3}, T. Balaganapathi¹, A. K. Poswal⁴ and H. K. Poswal^{1,3,*}¹High Pressure and Synchrotron Radiation Physics Division, Bhabha Atomic Research Centre, Mumbai 400085, India²Chemistry Division, Bhabha Atomic Research Centre, Mumbai 400085, India³Homi Bhabha National Institute, Anushaktinagar, Mumbai 400094, India⁴Atomic & Molecular Physics Division, Bhabha Atomic Research Centre, Mumbai 400085, India (Received 19 May 2023; revised 23 August 2023; accepted 30 October 2023; published 22 November 2023)

The high-pressure (HP) behavior of the tetragonal phase of $Y_{1.8}Eu_{0.2}Ge_2O_7$ has been studied using x-ray diffraction, x-ray absorption spectroscopy, Raman, and photoluminescence spectroscopy techniques. Our studies show pressure-induced amorphization in $Y_{1.8}Eu_{0.2}Ge_2O_7$ accompanied by partial transformation to a crystalline phase above ~ 14.0 GPa. Simultaneous high-pressure–high-temperature (HP-HT) experiments confirm the pyrochlore structure of the high-pressure crystalline phase. These structural transformations have been explained in terms of the coordination change at both of the cation sites as observed with x-ray absorption near-edge structure analysis of the Y edge, and extended x-ray absorption fine-structure analysis of the Ge edge. These inferences are also complemented by Raman spectroscopy, where the observed broadening and softening of GeO_4 tetrahedra stretching Raman modes above 14 GPa are suggestive of distortion and coordination change at Ge sites. High-pressure photoluminescence studies show a gradual evolution to a relatively more symmetric environment, and the emergence of two different site symmetries for Eu^{3+} ions with pressure. At 13.4 GPa, two new emission lines appear at 579.3 and 585.2 nm, which correspond to $^5D_0 \rightarrow ^7F_0$ and $^5D_0 \rightarrow ^7F_1$ transitions in the transformed phases of the compound. After pressure cycling up to ~ 24 GPa, the system undergoes complete amorphization upon pressure release in the case of ambient temperature HP studies, whereas the pyrochlore phase is retained upon pressure release in the case of HP-HT studies. These studies demonstrate the quenchability of higher coordinated crystalline and amorphous phases at ambient conditions in this system depending on the pressure cycling pathway, which may be useful in the study of exotic magnetic phases in this system.

DOI: [10.1103/PhysRevB.108.174108](https://doi.org/10.1103/PhysRevB.108.174108)**I. INTRODUCTION**

Rare-earth pyrogermanates ($Re_2Ge_2O_7$) have been a subject of fundamental interest due to their geometrically frustrated spin lattice, which exhibits novel ground states such as spin ices, spin glasses, and spin liquids [1–4]. The rare earth pyrogermanates act as magnetic ions, and their interaction with the local crystal-field results in short-range magnetic ordering showing spin ice behavior, which has been suggested to be the most promising candidate for realizing magnetic monopoles [5]. Their magnetic property is controlled by the ratio of magnetic exchange and dipolar interaction of the nearest-neighbor spins. This ratio can be tuned either by chemical pressure or by the application of external pressure. In fact, Zhou *et al.* [6] reported that increasing the chemical pressure drives the system toward the spin-ice–antiferromagnetism phase boundary. In another study by Mirebeau and Goncharenko, pressure-induced long-range antiferromagnetic behavior was reported. Dipolar interaction is very sensitive to the distance between magnetic ions, and it can lead to the realization of various magnetic phase transitions due to local structural modifications. It is therefore evident that the crystalline structure and hence the magnetic

ion local symmetry plays a vital role here, and [7–9] different structures of these pyrogermanates may lead to further enhancement of dipolar interactions, leading to new physics [10,11].

The crystalline structure of the pyrogermanates is sensitive to the ionic radius ratio (RR) (r_{Ln}^{+3}/r_{Ge}^{+4}), which can be modified by changing the rare-earth elements or subjecting them to extreme pressures. Depending on the RR, $Re_2Ge_2O_7$ (RGO) can be synthesized in triclinic ($Ln = La, Pr, Nd, Gd$), hexagonal ($Sm_2Ge_2O_7$ and $Gd_2Ge_2O_7$), and tetragonal ($Gd-Lu$) structures [12]. Other probable structures with similar chemical compositions are pyrochlore or defect fluorite. However, under ambient conditions, $Re_2Ge_2O_7$ with $RR > 1.84$ cannot be synthesized in pyrochlore structure [13] as the criterion for stability of pyrochlore structure is empirically $1.36 < RR < 1.71$. However, with high pressures, the stability region of a pyrochlore lattice can be extended up to $RR \sim 2.30$ [14]. There have only been a few high-pressure studies on pyrogermanates so far. In one such study, hexagonal pyrogermanates, such as $Sm_2Ge_2O_7$ and $Gd_2Ge_2O_7$, have been reported to transform to pyrochlore phase under pressure [15], whereas tetragonal $Ho_2Ge_2O_7$ was shown to undergo pressure-induced amorphization (PIA) [16]. These studies suggest that tetragonal pyrogermanates with higher RR are more likely to undergo amorphization under pressure. The mechanism of PIA in $Ho_2Ge_2O_7$, as suggested by Li *et al.*, is due to the

*himanshu@barc.gov.in

breaking-up of the long chains of the edge-shared polyhedron group Ho_4O_{20} [15]. The mechanism of PIA, however, may vary in different systems depending on stress state, strain rates, and type of interatomic interactions ranging from covalent, ionic, Van der Waals, to hydrogen bonds [17–21].

High-pressure amorphization is understood in terms of a kinetically arrested phase during transformations to metastable systems, polyhedral orientation disordering, or pseudomelting, and it has been extensively studied [22–24]. This kinetic barrier can be overcome by heating the system under pressure in the Laser Heated Diamond Anvil Cell facility. This leads to the complete removal of the amorphous phase, and it drives the system to adopt a more stable crystalline phase. Thus although there are extensive studies on the driving mechanism of PIA, little has been dedicated to studying local structural changes during PIA.

It is worth mentioning here that in the pyrochlore structure ($Fd\bar{3}m$) of $\text{Re}_2\text{Ge}_2\text{O}_7$, which shows exotic spin states, Re and Ge are eightfold- and sixfold-coordinated, respectively. Both of the cations are located at the vertices of two distinct corner-sharing tetrahedrons, and the magnetic property of the rare-earth ion leads to the magnetic frustration in the lattice [25]. In contrast with this, the tetragonal form ($P4_32_12$) of RGO, despite having low (C_1) point-group symmetry of the rare earth, also shows highly anisotropic magnetic susceptibilities. Geometrical frustration arises from the spiral of the alternating edge- and corner-sharing rare-earth triangles, which is almost parallel to the fourfold symmetry axis of the tetragonal structure [1]. Under application of an external magnetic field, they show local Ising-like magnetic behavior. A disordered pyrochlore or defect fluorite structure has also been found to show high-temperature spin freezing with the application of an external field by slowing down the spin dynamics [26,27].

In this manuscript, we have taken up the tetragonal phase of $\text{Y}_2\text{Ge}_2\text{O}_7$ as a host and doped it with 10% of Eu^{3+} ions at the site of Y^{3+} ions. Since Y^{3+} ions are nonmagnetic in nature, we have replaced a few of them by Eu^{3+} , which shows exceptional magnetic susceptibility due to the close separation between ground state 7F_0 and first excited state 7F_1 levels [28,29]. Doping with Eu^{3+} ions has another advantage in that its emission characteristics directly reflect its crystal-field environments, which can be used to probe the local site symmetry changes around Y^{3+} ions. We have performed a detailed structural investigation on $\text{Y}_{1.8}\text{Eu}_{0.2}\text{Ge}_2\text{O}_7$ under high pressures employing various local as well as long-range probing techniques, viz., x-ray diffraction, x-ray absorption spectroscopy, Raman scattering, and photoluminescence spectroscopy. These high-pressure studies on $\text{Y}_{1.8}\text{Eu}_{0.2}\text{Ge}_2\text{O}_7$ may be quite useful in understanding the complex magnetic phase space of rare-earth pyrogermanates, and they can be explored for possible spin ice, spin liquid, and spin glass behavior.

II SYNTHESIS AND CHARACTERIZATION

$\text{Y}_{1.8}\text{Eu}_{0.2}\text{Ge}_2\text{O}_7$ (YGOE) was prepared by the standard solid-state synthesis method. The complete details of the synthesis have been mentioned elsewhere [30].

The characterization of YGOE was done at extreme conditions x-ray diffraction (ECXRD) beamline

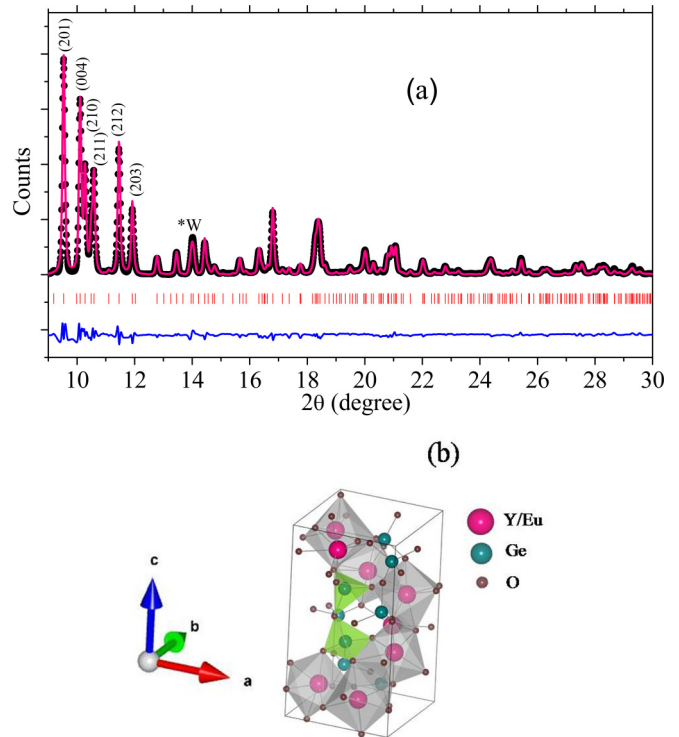


FIG. 1. (a) Rietveld refined x-ray diffraction pattern of the tetragonal phase of $\text{Y}_{1.8}\text{Eu}_{0.2}\text{Ge}_2\text{O}_7$ at ambient pressure inside a diamond anvil cell. The solid circle denotes the experimental data, while the solid pink line is a calculated pattern. The blue line denotes the residual of the refinement. Vertical tick marks correspond to Bragg peak positions for the sample. Miller indices of a few diffraction peaks from the sample have also been indicated. (b) Crystal structure of the tetragonal phase of YGOE. Atoms are represented in pink, green, and brown for Y, Ge, and O atoms, respectively. The wavelength of the x-ray beam used is 0.5458 Å.

(BL-11), Indus-2, synchrotron radiation source, India [31]. The pattern of the x-ray diffraction experiment at ambient pressure on YGOE is shown in Fig. 1(a). The pattern can be indexed with tetragonal space group $P4_32_12$. The Rietveld refined unit-cell parameters are $a = 6.8055(1)$ Å, $c = 12.3787(1)$ Å for YGOE. This is in good agreement with the values reported in the literature [30,32].

The structure of YGOE showing its constituent polyhedra is shown in Fig. 1(b). It has four formula units in its unit cell. The tetragonal structure of YGOE consists of YO_7/EuO_7 polyhedra and Ge_2O_7 units, which are composed of oxygen-sharing GeO_4 distorted tetrahedra at the corners. The coordination polyhedron of the $\text{Y}^{3+}/\text{Eu}^{3+}$ ion is a distorted pentagonal bipyramid with the $\text{Y}^{3+}/\text{Eu}^{3+}$ ion located nearly in the basal plane. The pentagonal bipyramids are edge-sharing and create a continuous YO_7/EuO_7 helical chain along the c -direction [16]. The refined structural parameters and various R factors, indicating the goodness of the fit at ambient pressure, are given in Table I.

III. EXPERIMENTAL DETAILS

For high-pressure studies, we have used a Mao-Bell-type diamond anvil cell (DAC), membrane DAC, and symmetric

TABLE I. The refined structural parameters and various R factors, indicating the goodness of the fit at ambient pressure, for YGOE.

YGOE			
R factor;			
$wRp = 0.02$, $Rp = 0.02$			
$a = 6.8055(1) \text{ \AA}$, $c = 12.3787(1) \text{ \AA}$			
$V = 573.307(0.021) \text{ \AA}^3$			
Atom	x	y	z
Y	0.3496(4)	0.8787(5)	0.6349(2)
Eu	0.3496(4)	0.8787(5)	0.6349(2)
Ge	0.0987(4)	0.8558(4)	0.3774(2)
O1	0.1244(21)	0.8755(21)	0.2500
O2	-0.0693(14)	1.0318(12)	0.3896(11)
O3	-0.0397(14)	0.7268(14)	0.4234(9)
O4	0.2827(12)	0.8654(27)	0.4510(6)

DAC for x-ray diffraction (XRD), Raman and photoluminescence spectroscopy, and x-ray absorption spectroscopy (XAS), respectively. A methanol:ethanol (4:1) mixture was used as a pressure-transmitting medium (PTM) in all the experiments. It has a hydrostatic limit of nearly 10.5 GPa [33]. For each experiment, a sample chamber was prepared by drilling a hole with a diameter nearly half the culet size in a preindented tungsten gasket.

High-pressure (HP) XRD data were collected at the ECXRD beamline (BL-11) at Indus-2 synchrotron. The ECXRD beamline at Indus-2 is a bending magnet based beamline that provides a usable flux of x-rays in the range of 5–25 keV and especially optimized for DAC-based *in situ* HP studies. For XRD experiments, the white synchrotron beam at the beamline was monochromatized to a wavelength of 0.5458 Å using a single-crystal Si (111) channel cut monochromator and microfocused to a spot size of $\sim 30 \mu\text{m} \times 30 \mu\text{m}$ (FWHM) at the sample stage with the help of a Pt-coated KB mirror system. For *in situ* pressure calibration, an equation of state of copper [34] was used, for which a few fine grains ($\sim 5 - 10 \mu\text{m}$) of copper were also loaded in the sample chamber along with the sample and PTM. The error in the pressure determination with the Cu diffraction pattern is < 0.1 GPa. The diffraction data were collected at an MAR345 image plate area detector. Dioptas software [35] was used to refine the sample to detector distance and detector tilt parameters using an XRD pattern of standard LaB_6 . Dioptas was also used to convert the two-dimensional partial rings obtained on the detector to one-dimensional patterns. These data were further processed with GSAS software to obtain structural parameters using the Rietveld refinement method [36].

HP-XAS measurements have also been carried out at BL-11, Indus-2. To perform the measurements, we have used the same sample environment as stated previously in HP-XRD. XAS data have been recorded in continuous-scan extended x-ray absorption fine structure (EXAFS) mode, described elsewhere in detail [37]. X-ray absorption near edge structure (XANES) and extended x-ray absorption fine structure have been recorded at the K edge of both Y atoms (17038 eV) and Ge atoms (11108 eV). Seven scans have been taken at

every pressure step at different orientations of DAC with 1° steps within the angle range of $\pm 3^\circ$ about the vertical axis of the diffractometer. It was then processed as per the iterative algorithm described by Hong *et al.* [38] to remove the glitches from the diamond and improve the signal-to-noise ratio. Energy calibration of the monochromator has been performed by collecting XAS data from Y metal foil. The edge position of Y foil (the maxima of the first derivative of the absorption data) was aligned to the actual value of the absorption edge, i.e., 17038 eV. The incident x-ray was measured using an Ar gas-filled ionization chamber. All data were processed using Athena software, and EXAFS data analysis was performed using FEFF6 and the Artemis program [39,40].

HP photoluminescence (PL) and Raman scattering experiments have been performed on a Jobin Yvon triple-stage T64000 Raman spectrometer in a backscattering geometry. We have used a Coherent make argon-ion laser wavelength of 488 nm and an He-Ne laser of 632.8 nm as an excitation source. The spectra are collected by a $20\times$ objective lens (Olympus, Japan) and recorded on a Peltier cooled charge coupled device detector. Spectra are recorded with a grating having 1800 grooves per mm, which provides the resolution of $< 2 \text{ cm}^{-1}$.

For high-pressure Raman experiments, pressure was estimated using the ruby fluorescence method [41]. For this, a ruby chip of size ~ 10 micron was loaded in DAC along with the powdered sample and PTM. The error in the pressure using ruby fluorescence is < 0.1 GPa. HP-PL measurements have been carried out using a membrane diamond anvil cell. To measure the pressure, a first-order Raman mode of diamond at the center of the culet has been taken [42]. The pressure distribution at the culet center is almost flat, and the error in pressure determination is < 0.66 GPa up to 100 GPa [43]. Ruby was not used for HP-PL studies due to the spectral overlap of its fluorescence with that of the sample.

IV. RESULTS AND DISCUSSION

A. High-pressure x-ray diffraction studies

HP XRD experiments on $\text{Y}_{1.8}\text{Eu}_{0.2}\text{Ge}_2\text{O}_7$ have been performed up to ~ 24.1 GPa. The XRD patterns of YGOE at selected pressure are shown in Fig. 2. As can be seen in the figure, all the peaks shift monotonously towards a higher 2θ value due to compression of the unit cell, and there is no anomalous behavior observed in the pattern below a pressure of 13.7 GPa. Both a and c lattice parameters decrease under pressure [Figs. 3(b) and 3(c)]; however, the c/a ratio varies nonmonotonously. First it decreases gradually by about 3% up to 8 GPa, and subsequently increases to ~ 1.8214 [Fig. 3(d)]. This shows higher compressibility of the c -axis below 8 GPa and the a axis above 8 GPa.

The change in the c/a ratio should be due either to anisotropic compressional behavior and its evolution under pressure in the system, or to the presence of differential stresses beyond solidification pressure of the pressure-transmitting medium. Typically the differential stress beyond the hydrostatic limit of the M:E::4:1 pressure-transmitting medium is less than 0.5 GPa below 13 GPa [33]. In addition, differential stresses should affect the c/a ratio only in the case

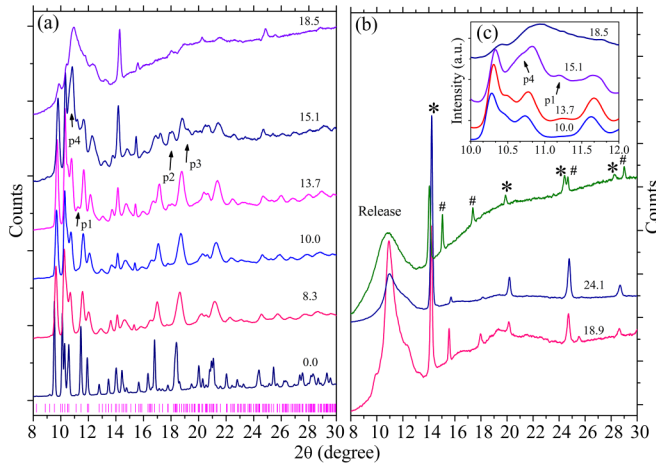


FIG. 2. (a), (b) Pressure evolution of XRD patterns of the tetragonal structure of $Y_{1.8}Eu_{0.2}Ge_2O_7$; (c) zoom-in view to show new emerging peaks $p1$ and $p4$. Diffraction peaks marked with “*” and “#” correspond to W and Cu, respectively. Pressure has been shown in GPa on the right side of the graph.

of significant preferred orientation. We did not observe any significant preferred orientation above 10 GPa, suggesting the predominant role of inherent compressional behavior in the observed c/a ratio changes. Nevertheless, the role of differential stresses may not be completely ruled out above 10 GPa.

Looking at the crystal structure of the tetragonal phase, the compression along the c -axis can be primarily associated with the bending of the Ge_2O_7 unit and the helical chain of the edge-shared polyhedron group Y_4O_{20} , and compression along

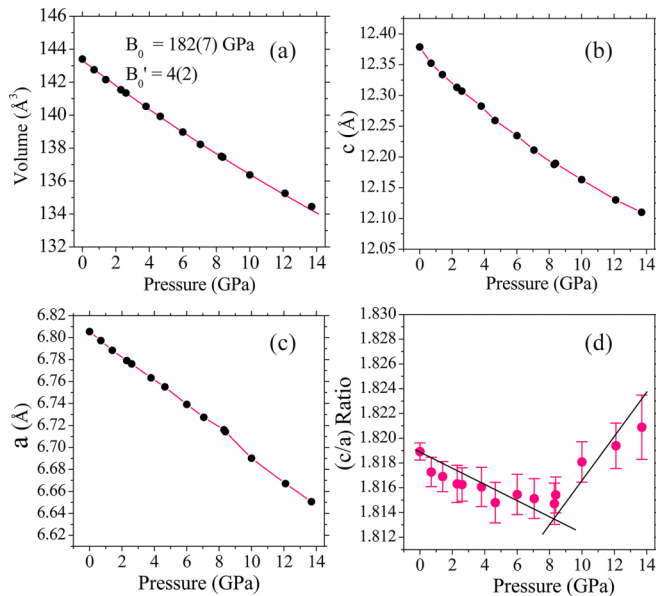


FIG. 3. All the data points belong to the tetragonal phase of YGOE. (a) Experimental pressure-volume data are shown by solid circles. Error bars are within the size of the symbols. The solid line represents the third-order BM-EOS fit to the experimental data. (b) Variation of c -axis and (c) a -axis of the unit cell with pressure. (d) The evolution of the c/a ratio with pressure. The straight line is a guide to the eyes.

the a and b axes should correspond to the compressibility of the YO_7 polyhedral unit. Under pressure, the observed nonmonotonous behavior of the c/a ratio could be due to the competing roles of the bending and compressibility of polyhedral units.

When pressure is increased to 13.7 GPa, a small diffraction peak ($p1$) is seen at $2\theta \sim 11.2^\circ$. When pressure is further increased to 15.1 GPa, a few more peaks, namely $p2$, $p3$, and $p4$, are observed at $2\theta \sim 17.9^\circ$, 19.2° , and 10.7° , respectively, which is indicative of the emergence of another crystalline phase. Apart from this, broad peak profiles due to the formation of a small fraction of amorphous states are also seen at this pressure.

When the sample is compressed beyond 17.5 GPa, the most intense peaks due to ambient phase (201) and (004) planes start to diminish and become very weak at 18.9 GPa. The sudden decrease in intensity of (201) and (004) suggests that the fraction of the ambient phase of YGOE is decreasing with pressure, and the fractions of new phases (crystalline and amorphous) are making a major contribution to the observed diffraction pattern. A similar concomitant crystal-to-crystal transition and amorphization under high pressures have also been reported in other systems [44]. With increasing pressure, the fraction of the amorphous phase increases, and at a pressure of 18.9 GPa, a clear broad hump is evident in the pattern. When the sample is further compressed to 21.8 GPa, the x-ray diffraction pattern indicates that all the peaks (except for sharp peaks due to tungsten and copper) get broadened and merge together, giving rise to an amorphouslike diffraction pattern. The same pattern is maintained at the highest pressure of the experiment, i.e., 24.1 GPa. When pressure is completely released from the sample, it undergoes complete amorphization [Fig. 2(b)]. Recently, another tetragonal pyrogermanate, $Ho_2Ge_2O_7$, has also been reported to undergo PIA under pressure and upon pressure release [16].

For an estimation of the bulk modulus of ambient phase, only P - V data below 10.5 GPa have been used, as the hydrostatic limit of PTM is 10.5 GPa. The data have been fitted with a third-order Birch-Murnaghan equation of state, and they are shown in Fig. 3(a). The values of the bulk modulus and its derivative at ambient pressure for YGOE are estimated as 182(7) GPa and 4(2), respectively. This is close to the value [$B = 193(4)$ GPa] for tetragonal $Ho_2Ge_2O_7$ [16].

When the pressure is released completely from YGOE, the system does not revert back to the ambient structure, hence the transformation is irreversible. This is contrary to $Ho_2Ge_2O_7$ [16], which has been reported to show reversible structural transformation under pressure. Due to the simultaneous existence of ambient and high-pressure phases in a pressurized state, the transformation is first-order in nature.

In the next step, we have tried to address the probable high-pressure crystalline phase of the compound. Our XRD pattern at 18.4 GPa has a similar appearance to that of $Gd_2Ti_2O_7$ [45,46] and pyrochlore $Gd_{2-x}Zr_xTi_2O_7$ [47] under pressure. The authors have described them as a distorted pyrochlore structure where either the cation or the cation sublattice is disordered, while the other maintains ordering as reflected by some sharp peaks in the XRD spectra [48]. So, at this point we claim that, most probably, the high-pressure crystalline phase of YGOE could be a distorted pyrochlore phase. However,

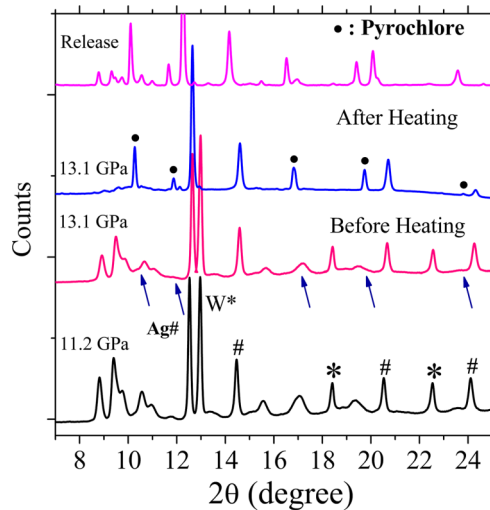


FIG. 4. Pressure evolution of XRD patterns of tetragonal $\text{Y}_{1.8}\text{Eu}_{0.2}\text{Ge}_2\text{O}_7$ before and after laser heating has been shown. New emerging peaks have been marked as arrows. Diffraction peaks marked as “•” correspond to the high-pressure pyrochlore phase ($Fd\bar{3}m$) of YGOE, while those marked as “*” and “#” belong to W and Ag, respectively. Pressure has been shown on the left side of the graph.

due to a larger fraction of amorphous phase at high pressures, Le Bail or Rietveld refinement of high-pressure diffraction patterns could not be performed with the pyrochlore phase.

Partial transformation to a crystalline phase and substantial amorphization under high pressures could be due to kinetic hindrances at ambient temperature. Hence to overcome the kinetic barrier, we have performed a simultaneous high-pressure–high-temperature experiment in the Laser Heated Diamond Anvil Cell (LHDAC) facility [49]. For this we compressed the system at a pressure ~ 13.1 GPa, and the sample was heated to $\sim 1350^\circ\text{C}$. The compound is white in color, and it could not directly couple with the IR laser for heating. For coupling we used silver powder, which was mixed with the compound. The XRD data after heating are shown in Fig. 4.

Heating led to the removal of all diffraction peaks of ambient tetragonal phase, and some new peaks appeared. It turns out that all the new peaks can be precisely indexed with the pyrochlore structure ($Fd\bar{3}m$) with a lattice parameter $a = 9.7220(5)$ Å. The remaining peaks in the pattern correspond to Ag, which was used as coupling material during laser heating. The Rietveld refinement of the pattern at 13.1 GPa is shown in Fig. 5. The volume discontinuity at this pressure is about 14%. When the pressure is completely released from the system, the release pattern shows some additional peaks. The additional peaks in the release diffraction pattern correspond to the ambient structure (tetragonal), which could have emerged from the unheated portion of the sample during laser heating. The laser focal spot size was ~ 3 μm , whereas the sample chamber was ~ 150 μm . The laser beam was scanned across the central portion in the range of ~ 50 μm only in order to avoid the gasket boundary. At high pressure, the diffraction pattern recorded by the small

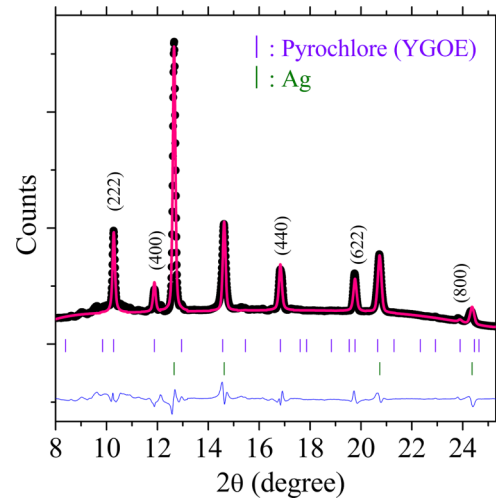


FIG. 5. Rietveld refined x-ray diffraction pattern of the pyrochlore phase of $\text{Y}_{1.8}\text{Eu}_{0.2}\text{Ge}_2\text{O}_7$ at 13.1 GPa pressure inside a diamond anvil cell after the laser heating at $\sim 1350^\circ\text{C}$. The solid circle denotes the experimental data, while the solid pink line is the calculated pattern. The blue line denotes the residual of the refinement. Vertical tick marks correspond to Bragg peak positions for the sample (violet) and Ag (green). Miller indices of diffraction peaks from the YGOE-pyrochlore structure have also been indicated. Goodness-of-fit parameters are $wRp = 0.06$, $Rp = 0.04$. Unit-cell parameters at 13.1 GPa are $a = 9.7220(5)$ Å, $V = 918.897(0.161)$ Å³. The wavelength of the x-ray beam used is 0.5031 Å.

size of the beam (FWHM ~ 30 μm) is from the heated sample portion showing the HP-HT phase, giving predominantly the pyrochlore phase. However, upon a complete release of pressure, due to the small movement of the sample chamber, some unheated sample also contributed to the diffraction pattern, giving rise to more intense peaks of the ambient phase. The presence of HP-HT peaks upon complete release of the pressure shows the irreversibility of this phase transition. The lattice parameter of the pyrochlore structure after release at ambient pressure is $a = 9.8965(4)$ Å. These observations are consistent with our conjecture of a distorted pyrochlore structure in ambient temperature HP studies. With sufficient energy in HP-HT conditions, the system could overcome the kinetic barrier for the first-order crystal-to-crystal transition from ambient tetragonal phase to the high-pressure pyrochlore phase. Incidentally, both the amorphous and HP pyrochlore phases are quenchable at ambient conditions depending on pressure cycling pathways.

It will also be interesting to discuss here the origin of the HP amorphous phase, which has been found to coexist with the HP crystalline phase. There may be two possible routes for the HP amorphous phase. The first is the direct transformation from tetragonal to amorphous, and the second is the tetragonal to pyrochlore to amorphous phase transition. Since tetragonal YGOE has the edge-shared polyhedron group Y_4O_{20} along the fourfold symmetry axis of the tetragonal structure, amorphization can be associated with the breaking-up of the long chains of Y_4O_{20} , similar to what is seen in $\text{Ho}_2\text{Ge}_2\text{O}_7$. In the second route, a pressure-induced amorphization mechanism may be associated with the energetics of various defect

formations in the compound, similar to that described for the other pyrochlore structures [50]. With this analogy, the new phase of YGOE has the tendency to form cation antisite and anion Frenkel defects. Because there is a large difference in the cation radii ratio ($r_{\text{Y}^{+3}}/r_{\text{Ge}^{+4}}$), defect formation energy is expected to be large [51]. This leads to an accumulation of point defects, which is reflected in terms of concomitant amorphization in the system [52]. When the number of defects formed exceeds the critical value, the system cannot revert back to the pyrochlore phase, and it undergoes complete amorphization upon the release of pressure. However, we do not comment on exactly what route the system is following to realize the amorphous phase. But it would be equally important to study here the evolution of the local structure around Y and Ge atoms under pressure, in particular the local coordination geometry of the amorphous phase. Therefore, in the next step, we have attempted to measure the coordination number changes around Y and Ge atoms when structural transformation is taking place in the system. Since the new crystalline phase is a distorted pyrochlore type, the usual eightfold- and sixfold-coordinated Y and Ge atoms, respectively, are expected. However, it will be interesting to see how the local coordination around the cations is evolved in the amorphous phase.

B. High-pressure x-ray absorption studies

Experimentally, the coordination number can be quantified with XAS measurements. Therefore, we carried out HP-XAS, mainly XANES and EXAFS of YGOE, to measure the coordination number of Y and Ge atoms, at BL-11 Indus-2. X-ray absorption spectroscopy provides information about the local structure around the central absorbing atom within a distance of ~ 5 Å.

1. High-pressure XANES at yttrium K-edge

Normalized high-pressure XANES data (shifted in the vertical axis) at Y *K*-edge are shown in Fig. 6. The spectra, shown here, consist of a single smooth broad absorption profile, and the first EXAFS oscillation is located at approximately 45 eV above the white line. The peak shape of the spectra is consistent with the earlier reported XANES data for the Y edge in different compounds [53]. The x-ray absorption cross section at the yttrium edge arises due to the electrical dipole transition $1s \rightarrow 5p, np$. XANES spectra are sensitive to the ligand, local coordination, and oxidation state of the absorbing atom. In fact, one can determine the local structural details by comparing XANES data of unknown samples with those of the known one. Therefore, in order to understand the correlation between the coordination number around the Y atom and its XANES spectral feature, we have also performed XANES measurement at the Y edge on Y_2O_3 (sixfold-coordination) and $\text{Y}_{1.98}\text{Eu}_{0.02}\text{Sn}_2\text{O}_7$ (eightfold-coordination) under ambient conditions. They have been used as a reference and compared with HP-XANES data at the Y edge in YGOE at different pressures. In Y_2O_3 , there are two nonequivalent Y atoms; one has a nearly regular octahedron environment of the ligand (C_{3i} site symmetry) while the other is at the center of distorted octahedron geometry (C_2 site symmetry). From the inspection of these patterns, it is evident that the spectra consist of the two distinguishable characteristic features

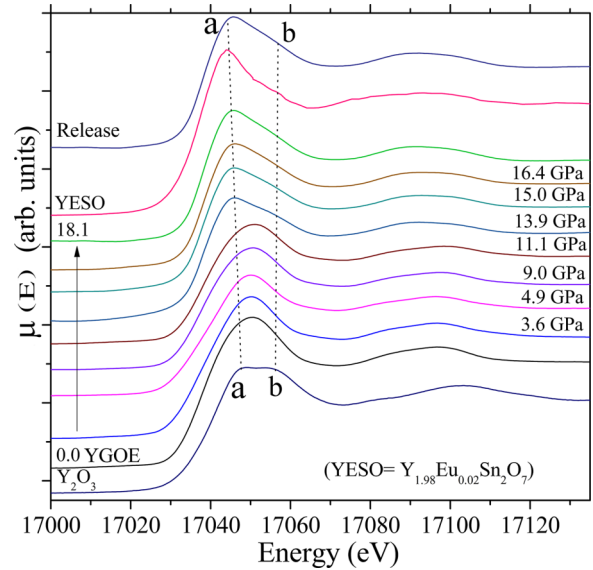


FIG. 6. Normalized XANES spectra (shifted in vertical axis) at the Y-edge in YGOE at various pressures. Pressures in GPa have been marked on the right of the data. “a” and “b” represent two features in the pattern. For comparison, two references, viz., Y_2O_3 and $\text{Y}_{1.98}\text{Eu}_{0.02}\text{Sn}_2\text{O}_7$ (YESO), at ambient pressure have also been shown. Y is sixfold-coordinated in Y_2O_3 while it is eightfold-coordinated in YESO.

marked as *a* and *b* in Fig. 6. They are located at ~ 10 and ~ 18 eV above the Y-edge (17 038 eV), respectively. In comparison, Y in YGOE is in sevenfold-coordination occupying low site symmetry (C_1), and shows a single broad peak at about ~ 12 eV above the Y-edge. This feature gets shifted towards higher energy upon compression due to the shortening of the bond length [54]. When pressure increases to 13.9 GPa, a clear change in the absorption profile can be seen. A new feature (*a*) emerges, located at approximately 8 eV above the edge, suggestive of structural transformation in the compound. $\text{Y}_{1.98}\text{Eu}_{0.02}\text{Sn}_2\text{O}_7$ pyrochlore has Y atoms occupying D_{3d} site symmetry with its XANES data showing higher intensity of the *a* feature located at about 8 eV above the Y-edge. The feature *b* is broadened and located at ~ 12 eV above the edge. This pattern resembles that of Y in YGOE at pressure ≥ 13.9 GPa. This suggests that the environment around Y in YGOE at higher pressure is similar to that in $\text{Y}_{1.98}\text{Eu}_{0.02}\text{Sn}_2\text{O}_7$, where Y is eightfold-coordinated. Therefore, we can conclude that the coordination number of Y is reflected in terms of the relative intensity of *a* and *b*, and Y becomes eightfold-coordinated under pressure in YGOE. Our results are consistent with a similar observation regarding the sensitivity of XANES spectral features and its relation to the coordination number of Y in several different compounds with various coordination geometries [53,55,56]. When the pressure is completely released from the sample, one can see that *a* has a higher intensity than *b*, which is consistent with the fact that the phase transformation is irreversible. We have presented here only the XANES data at the Y edge because HP EXAFS data had large diamond glitches and it was difficult to analysis them.

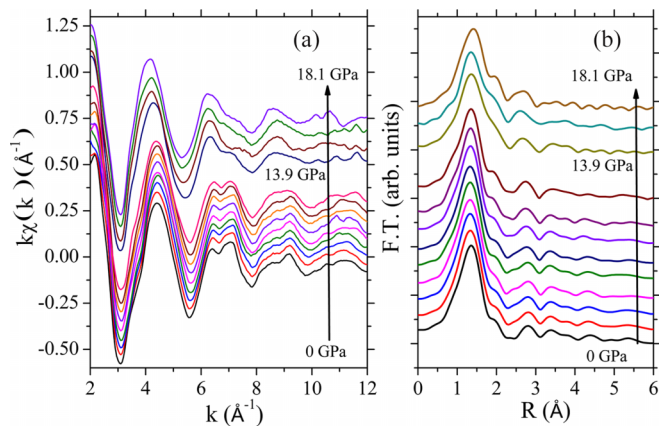


FIG. 7. (a) Evolution of Ge-edge XAS extracted $k\chi(k)$ signals (vertically shifted) with pressure. (b) Moduli of the Fourier transform of the experimental EXAFS spectra as the pressure increases.

2. High-pressure EXAFS at germanium K-edge

The EXAFS signal $\chi(k)$ was obtained by pre-edge background subtraction from the measured absorption coefficient and normalizing the EXAFS oscillation by the edge step. The plot of $k\chi(k)$ as a function of pressure is shown in Fig. 7(a). The pseudo radial distribution function around the absorbing embedded atom was obtained by Fourier transformation of the extracted signal using a Hanning window in the k range of 2–12 \AA^{-1} . The moduli of the Fourier transform are also shown with pressure in Fig. 7(b). Performing HP-XAS measurement with DAC is challenging due to Bragg's diffraction peaks from the diamond anvils, which limit the extent of the usable k range. From Fig. 7(a), it is evident that as the pressure increases, EXAFS oscillation shifts towards higher k values. This is mainly due to the compression of the bond length by the application of pressure. However, when the pressure is increased to 13.9 GPa, the first oscillation clearly shifts towards lower k values with pressure, and discontinuity is clearly evident at $P \geq 13.9$ GPa. Similar behavior is also observed for the second EXAFS oscillation. This is strong evidence for the structural transformation in the compound at pressure ~ 13.9 GPa.

A quantitative analysis of the high-pressure EXAFS data at the Ge edge has been performed using the ARTEMIS package [39,40]. The calculation of backscattering amplitudes and phases was carried out using the FEFF6 code. We have considered two known structural models for the local structure around Ge atom in $\text{Y}_{1.8}\text{Eu}_{0.2}\text{Ge}_2\text{O}_7$. The first is based on the crystalline phase of $\text{Y}_2\text{Ge}_2\text{O}_7$ in the tetragonal (fourfold-coordinated) phase, and second is the rutile structure (sixfold-coordination). The tetragonal structure possesses four oxygen atoms around Ge atoms at two different distances. In contrast, the local structure around Ge in rutile has a (2+4)-type double distance distribution of six oxygen atoms in [Ge-O] polyhedra. As stated previously, diamond glitches put a constraint on the k range of the data, thus we have only taken the first shell Ge-O path in the modeling. All the fittings were performed with a fixed value of the coordination number. We have thus tested three models: the first model had fourfold-coordination ($N=4$) and an average bond distance

TABLE II. Values of reduced chi square χ_v^2 and σ^2 obtained at selected pressures using four, five, and six coordination models for YGOE.

P (in GPa)	$N=4$		$N=5$		$N=6$	
	χ_v^2	σ^2	χ_v^2	σ^2	χ_v^2	σ^2
9	180	0.002	720	0.007	1440	0.009
18	828	0.005	234	0.006	340	0.008

of 1.81 \AA ; the second model had sixfold-coordination ($N=6$) and an average bond distance of 1.90 \AA ; the third model had fivefold-coordination, which we tested by taking the Ge-O distance with respect to the sixfold-coordinated model and setting $N=5$. EXAFS measurements have large uncertainties in the determination of the coordination number. Therefore, in order to clearly differentiate the coordination number changes around the Ge atom at ~ 14 GPa, we have fitted the experimental data at 9 and 18 GPa, with all three models based on fourfold-, fivefold-, and sixfold-coordination geometry. We have used reduced $\chi^2(\chi_v^2)$ as a relevant parameter to determine which of the models gave the best fit to the observed profile at 9 and 18 GPa. The value of χ_v^2 has been tabulated in Table II. It is clear that at 9 GPa, the fourfold-coordination model gave the best fit to the experimental data points, while at ~ 18 GPa, the fourfold-coordination model can definitely be ruled out. However, there is a small difference between the fivefold- and sixfold-coordination models. This may be due to the fact that in a distorted pyrochlore-type structure, anions are disordered, leading to a large variation in GeO_6 octahedral bond distances. Therefore, the coordination geometry around Ge is highly distorted. This suggests that the high-pressure phase is indeed a distorted pyrochlore-type structure.

Based on these refinements, it is evident that up to 12.5 GPa, the fourfold-coordination model gave the best fit to the experimental data points. The amplitude reduction factor parameter S_0^2 (0.9) has been kept constant over the whole pressure range and taken from the ambient data fitting [57]. We have only refined the values of the Ge-O bond distance and mean-square relative displacement σ^2 . Figure 8 represents the best fit between experimental data and the fitted curve using the fourfold-coordination model at a pressure of 9.0 GPa. When the pressure is increased to 13.9 GPa, experimental data can no longer be fitted by the fourfold-coordination model within the meaningful refinement parameters. It turns out that the fivefold- and sixfold-coordination models both give comparable best fitting to the experimental data points. However, for a comparison between experimental data and the best fit at the highest pressure of the experiment, i.e., at 18.1 GPa, the sixfold-coordination model has been shown in Fig. 9.

In the next step, the pressure evolution of the Ge-O bond distance has also been shown in Fig. 10(a). It is worth mentioning here that the Ge-O bond length is not affected by the variation in the EXAFS oscillation amplitude, and hence it is unaffected by changes in the sample thickness under pressure [58]. To represent the Ge-O bond length, we have divided it into two regions, shown as I and II in Fig. 10(a). Region I ($P < 13.9$ GPa) belongs to the ambient tetragonal phase, while region II ($P \geq 13.9$ GPa) belong to the sixfold-coordinated

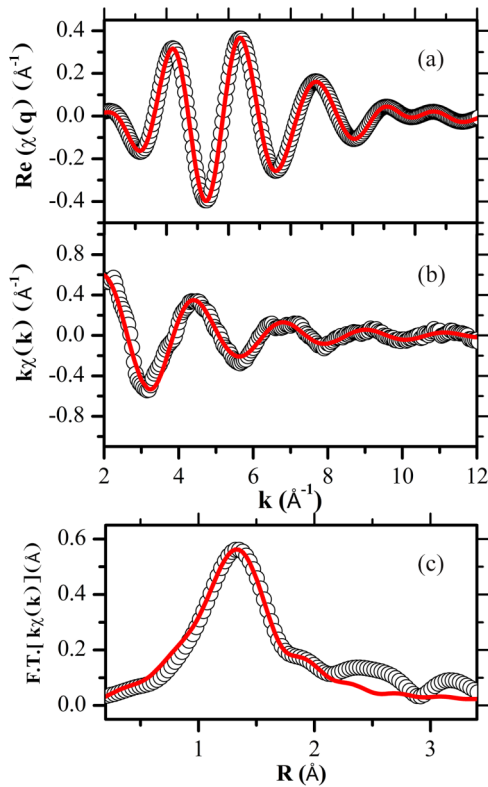


FIG. 8. Comparison between the experimental Ge-edge EXAFS spectrum (shown by circles) at 9.0 GPa and model calculation (shown by the solid curve) corresponding to a single-distance shell is reported for (a) the back-transformed signal, (b) the extracted $k\chi(k)$ signal, and (c) the moduli of the Fourier transforms.

distorted pyrochlore phase. Figure 10(a) suggests that the bond length initially decreases with pressure in region I. However, when the pressure is increased to 13.9 GPa, the system can best be described by the sixfold-coordination model, leading to an abrupt jump in the Ge-O bond distance. This jump is expected due to the volume discontinuity, which is a signature of the first-order structural transformation. The average Ge-O bond length in sixfold-coordination is approximately 1.90 Å, and this result is consistent with several studies on various germanium oxide compounds in which a fourfold- to sixfold-coordinated Ge atom has been reported by HP EXAFS measurements [59,60]. Debye-Waller factor σ^2 values with pressure have also been shown in Fig. 10(b). An increase in σ^2 with pressure is evident up to 13.9 GPa, which is understood in terms of an increase in static disorder within the system arising due to the onset of structural phase transformation [59,61]. This also causes an increase in coordination number of germanium in the HP phase, leading to a higher Ge-O bond distance, which further increases the Debye-Waller factor.

We have thus established from x-ray absorption measurements that when pressure is increased to ~ 13.9 GPa, the local coordination environment around Y increases from sevenfold- to eightfold-coordination, while for Ge atoms, fivefold- and sixfold-coordination models give reasonable fits to the observed pattern. This is maintained until 18.1 GPa. These results are in agreement with the inference of a distorted pyrochlore-type structure at high pressures from x-ray

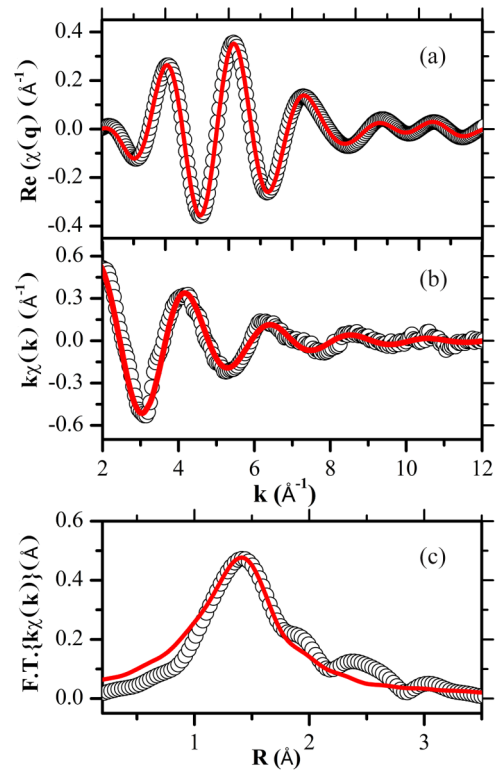


FIG. 9. Comparison between the experimental Ge-edge EXAFS spectrum (shown by circles) at 18.1 GPa and the model calculation (shown by the solid curve) corresponding to a single-distance shell is reported for (a) the back-transformed signal, (b) the extracted $k\chi(k)$ signal, and (c) the moduli of the Fourier transforms.

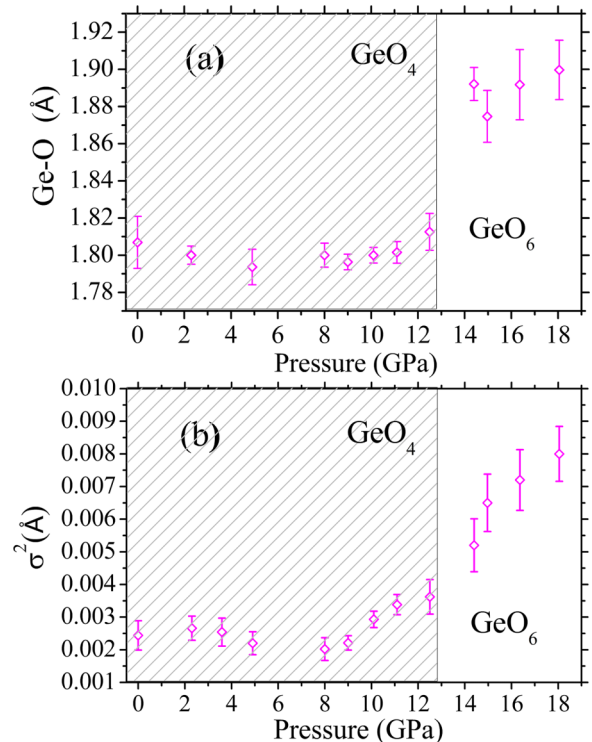


FIG. 10. (a) Evolution of Ge-O distance and (b) σ^2 parameter as a function of pressure.

diffraction measurements. It also needs to be pointed out here that at 18.1 GPa, the system has a large amorphous phase (noted from the x-ray diffraction measurements). Therefore, we can conclude that the local coordination around the Y and Ge atoms in the amorphous phase is similar to that in the distorted pyrochlore phase. This is an important observation because an eightfold-coordinated rare-earth ion in a typical pyrochlore structure is responsible for geometrical frustration in such a lattice, leading to interesting magnetic phase transitions. Pressure thus provides an opportunity to tune tetragonal to pyrochlore structure through an intermediate distorted pyrochlore phase. There have been reports that disorder in a pyrochlore structure leads to an absence of spin ice, but it shows spin freezing or spin liquid under application of a magnetic field [62,63]. In another study, anion disordering in the pyrochlore lattice induces a spin liquid state by freezing magnetic degrees of freedom, which shows quantum entanglement [64,65]. Therefore, structural disordering plays an important role in spin dynamics and spin-spin spatial correlation [66], and hence the structural modifications under high pressures in our sample provide a unique opportunity to investigate such behavior.

C. High-pressure Raman scattering studies

In the next step, we performed a Raman scattering experiment to study the local ordering in the system. It can provide local structural information in the range of 10–100 Å. $Y_{1.8}Eu_{0.2}Ge_2O_7$ has a tetragonal structure with space group $P4_32_12$. It has four formula units in its unit cell. Factor group analysis suggests a total of 132 Γ -point phonon modes [67]:

$$\Gamma_{\text{Total}} = 16A1 + 17A2 + 17B1 + 16B2 + 33E.$$

Raman-active modes are

$$\Gamma_{\text{Raman}} = 16A1 + 17B1 + 16B2 + 32E.$$

There are also IR-active modes:

$$\Gamma_{\text{IR}} = 16A2 + 32E.$$

Acoustic vibrations are represented as

$$\Gamma_{\text{acoustic}} = A2 + E.$$

Out of these, we have identified 27 Raman peaks. The Raman spectra of YGOE at ambient pressure are shown in Fig. 11. Raman peak frequencies and their FWHM have been fitted with the help of Origin software using a least-squares method and a Lorentzian peak profile function, and they are presented in Table III. This is also consistent with other similar compounds of the type $Ln_2Ge_2O_7$ ($Ln = Tb-Er$) with a tetragonal structure [67]. The Raman modes of tetragonal YGOE have been identified with the help of the literature [68,69]. There are fluorescence peaks seen in YGOE with excitation from a red laser. These peaks have been marked with an asterisk and they correspond to the $^5D_0 \rightarrow ^7F_3$ transition.

Raman modes in the frequency region $\nu > 400 \text{ cm}^{-1}$ are assigned to the internal modes (stretching and bending) of a GeO_4 tetrahedron [70]. Raman modes in the frequency region $\nu > 700 \text{ cm}^{-1}$ correspond to the various stretching vibrations of the GeO_4 tetrahedron. They are classified as symmetric and antisymmetric with respect to the local ternary axis of the GeO_3 unit. There can be in-phase or out-of-phase vibration. The antisymmetric bending vibrations of the GeO_3 unit (rep-

resented as δ_{as}) are relatively pure, but the corresponding symmetric modes are probably mixed with other vibrations [68].

Between the bending and stretching vibrations of a GeO_4 molecule, there is well-defined bridge symmetric stretching ν_s (Ge-O-Ge). There are four units of $(Ge_2O_7)^{6-}$ in a primitive lattice, thus it is expected to show four different vibrational frequencies corresponding to each unit. However, only two such modes are observed, while the remaining two are too small to be seen. The low-frequency region $\nu < 372 \text{ cm}^{-1}$ encompasses complex translations of both Y/Eu and Ge atoms and the mixing of some translational and rotational modes.

The HP Raman scattering experiments on YGOE have been performed using a 488 nm wavelength excitation source up to ~ 23 GPa. The Raman pressure evolution is shown in Fig. 12. With an increase in pressure, all the peaks shift towards the higher frequency region, as expected due to the lattice compression. The hydrostatic limit of our PTM is 10.5 GPa. Above this pressure, off-diagonal components of the stress tensor also cause some broadening in the profile. There are no other changes in the Raman spectra until 14 GPa, suggesting that the ambient tetragonal structure remains stable until then. We have fitted the evolution of Raman modes with pressure with a linear equation (shown in Fig. 13), and we calculated the linear pressure coefficients of all the modes. The values have been tabulated in Table III along with Grüneisen parameters γ given as $\gamma = (\frac{B_0}{\omega_0}) \times (\frac{\partial \omega}{\partial P})$, where B_0 is the ambient pressure bulk modulus, and ω_0 is the ambient Raman mode frequency. The value of B_0 was taken from the HP-XRD measurements. All the modes show positive pressure coefficients, and there is no mode crossover within the entire pressure range studied.

When the pressure is increased further to 14.0 GPa, there is a clear modification in the relative intensities of $\nu_{as}(GeO_3)$ modes, marked as an arrow in Fig. 12. It is even more pronounced when the sample is compressed to 14.9 GPa. At

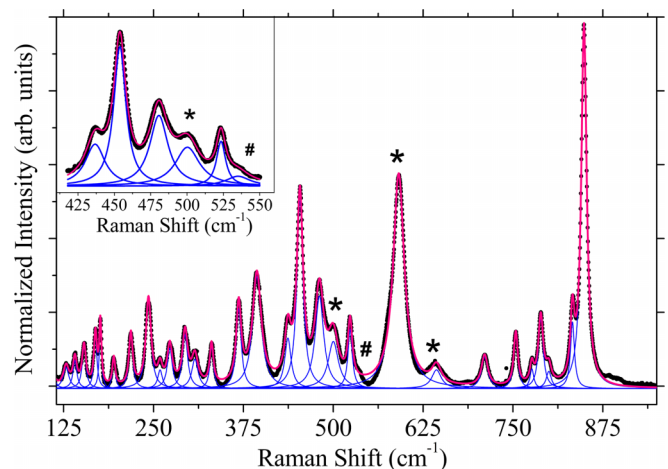


FIG. 11. Raman spectrum at ambient conditions of $P4_32_12$ phase of $Y_{1.8}Eu_{0.2}Ge_2O_7$. He-Ne laser of wavelength 632.8 nm is used for excitation. The observed data are represented by black circles. Individual fitted peaks are shown by blue. The convoluted profile has been shown by a solid red line. The symbol “#” represents the Raman line, which has been fitted separately regional-wise and shown in the top of the figure, and “*” represents the fluorescent line.

TABLE III. Fitted Raman modes of YGOE have been tabulated at ambient pressure. The FWHM has also been calculated at ambient pressure and shown in the column. The slope of each mode with pressure ($\frac{d\omega}{dP}$) and mode Grüneisen parameters γ has been calculated and tabulated against each.

	YGOE	FWHM	$d\omega/dP$	γ
1	128	9.60	0.18	0.26
2	141	6.52	0.29	0.37
3	153	6.44	0.18	0.21
4	169	4.99	0.10	0.11
5	176	3.70	0.17	0.18
6	195	4.78	1.04	0.97
7	$\nu(Y-O) + \rho(GeO_3)$	218	6.22	0.28
8	+lattice vibrations	243	8.67	0.71
9		259	7.65	1.81
10		273	8.49	1.14
11		294	8.62	1.20
12		307	10.51	2.09
13		331	6.08	0.45
14	$\delta_s(GeO_3)$	368	8.35	2.79
15		394	14.62	2.56
16		437	10.57	2.40
17	$\delta_{as}(GeO_3)$	454	10.15	3.15
18		481	14.28	3.18
19	$\nu_s(Ge-O-Ge)$	523	7.26	2.37
20		535	20.18	2.53
21		710	10.40	4.30
22		754	6.64	4.68
23	$\nu_{as}(GeO_3)$	776	6.39	4.63
24		788	8.04	5.19
25		800	8.60	4.71
26		833	6.65	4.27
27	$\nu_s(GeO_3)$	849	8.92	4.46

this pressure, most of the peaks in the region $<370\text{ cm}^{-1}$ corresponding to the cation vibration have disappeared. This is strong evidence for the onset of a structural phase transformation in the compound at a pressure ~ 14 GPa. The observation of a bridge symmetric stretch $\nu_s(Ge-O-Ge)$ mode is a signature of the presence of a pyro group in the compound [71]. Until 14.9 GPa, this mode (ν_s) remains visible, implying the existence of a tetragonal phase. As the pressure is increased above this, ν_s gets broadened completely and disappears above ~ 15.9 GPa. This suggests that the system does not contain any pyro group thereafter.

It is further observed that at a pressure ~ 17 GPa, all the peaks corresponding to the GeO_3 stretching vibration in the region $>675\text{ cm}^{-1}$ merge with each other, after which a broad feature is seen in the spectrum centered around 817 cm^{-1} . We have plotted the position of this broad profile against the pressure in Fig. 14. There is a mode softening of GeO_3 stretching vibration with pressure suggesting a probable increase in the bond length. This increase may be associated with the increase of the coordination number of the Ge atom due to the structural phase transformation. This is indeed due to the increase of coordination of the Ge atom from fourfold to sixfold under pressure as suggested by the HP XAS measurements.

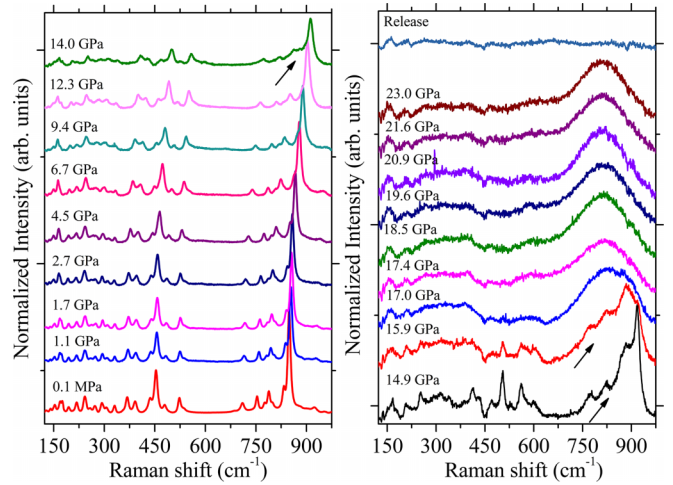


FIG. 12. Raman spectra of $Y_{1.8}Eu_{0.2}Ge_2O_7$ (excitation source 488 nm) at a few selective pressures. Pressure values have been shown on the left side of the figure.

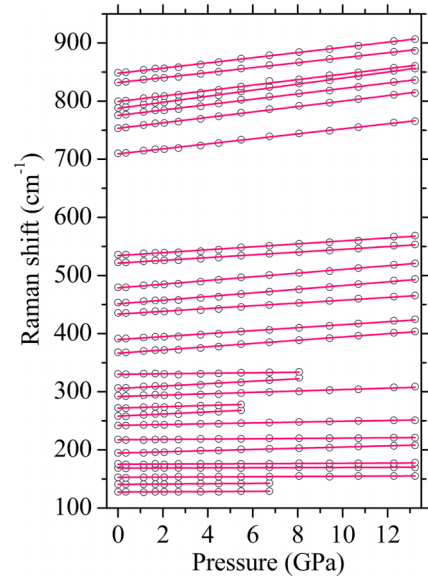


FIG. 13. Variations in Raman shift of $P4_321_2$ phase of $Y_{1.8}Eu_{0.2}Ge_2O_7$ with pressures. Experimental points have been shown by circles. The fitted line has been shown by solid lines.

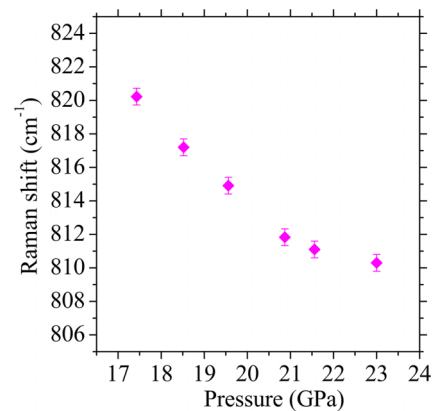


FIG. 14. Variations in Raman shift of the asymmetric stretching mode of $Y_{1.8}Eu_{0.2}Ge_2O_7$ with pressures.

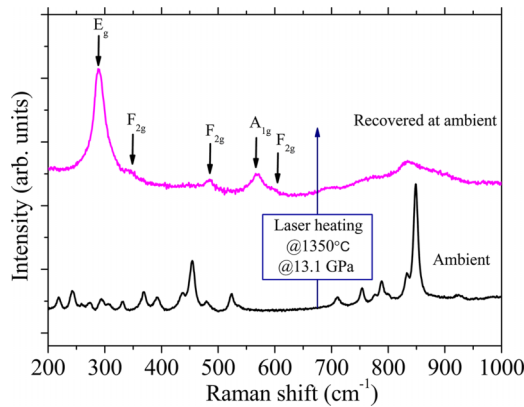


FIG. 15. Raman spectra of the ambient tetragonal phase of $Y_{1.8}Eu_{0.2}Ge_2O_7$ (excitation source 488 nm) in comparison with the recovered sample after laser heating at 13.1 GPa at temperature $\sim 1350^\circ\text{C}$. Newly emerged peaks marked as vertical arrows in the figure correspond to the high-pressure pyrochlore phase.

The broad feature observed at about $\sim 800\text{ cm}^{-1}$ also has an alternate interpretation. In a report, Zhang *et al.* [45,46] found that $Sm_2Ti_2O_7$ at ~ 33.8 GPa, when its pyrochlore structure gets disordered, develops a broad peak with a center frequency at $\sim 800\text{ cm}^{-1}$. $Gd_2Ti_2O_7$ develops the same broad peak at ~ 26.8 GPa, centered at 780 cm^{-1} in its distorted pyrochlore form. Hence our findings are in line with the x-ray diffraction and XAS analysis. Thus, the ambient phase becomes unstable above a pressure of ~ 14 GPa, and it shows a tendency to undergo transformation into a distorted pyrochlore-type structure. When pressure is completely released from the sample, we do not get any Raman scattering peak. Hence the sample can be said to undergo complete amorphization upon release, in accordance with the HP XRD measurements.

We have shown explicitly by x-ray diffraction measurements on the heated sample compressed at ~ 13.1 GPa that it forms an ordered pyrochlore structure. This is confirmed by Raman spectroscopic measurements on the heated sample. Figure 15 shows the Raman scattering data of the recovered sample after heating the sample under pressure at about 13.1 GPa. After heating the sample, a few new peaks emerge, as expected. These new peaks can be attributed to the well-known pyrochlore structure, which can be expressed as follows:

$$\Gamma = A_{1g} + E_g + 4F_{2g}.$$

All the new peaks have been identified and marked in Fig. 15.

Out of six modes, we have detected five of the pyrochlore structure, which appear at $290 (E_g)$, $345 (F_{2g})$, $485 (F_{2g})$, $569 (A_{1g})$, and $601 (F_{2g})\text{ cm}^{-1}$. The mode assignment has been done from the literature [46,72]. A_{1g} and E_g modes arise due to the movement of oxygen atoms sitting at the $48f$ site, while for F_{2g} mode, both $48f$ and $8a$ oxygen atoms contribute. The strongest mode at ~ 290 and $\sim 345\text{ cm}^{-1}$ represents O-Y-O bending vibration. Another band at $\sim 569\text{ cm}^{-1}$ is assigned to GeO_6 octahedra bending vibration. It is thus evident that the new high-pressure crystalline phase is a pyrochlore-type structure.

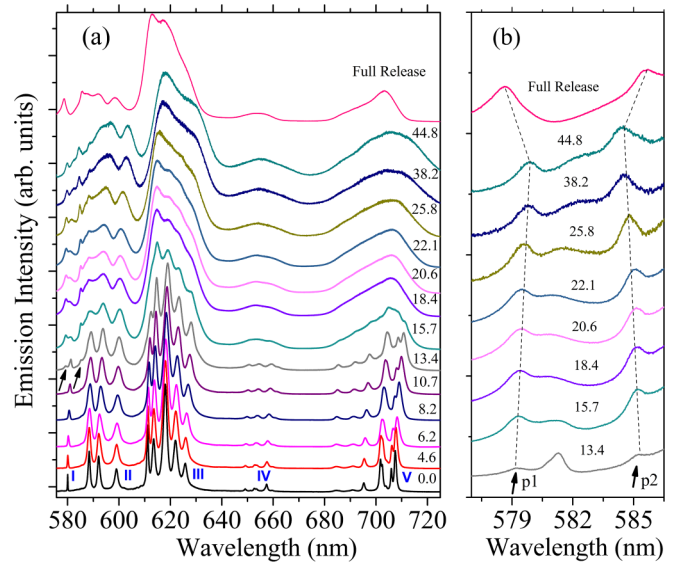


FIG. 16. (a) Photoluminescence spectra of $Y_{1.8}Eu_{0.2}Ge_2O_7$ at a few selective pressures (excitation wavelength 488 nm). (b) Zoom-in view at a few pressures showing the emergence of new peak positions and their pressure gradient. The values of pressure in GPa are shown on the right side of graph. Five bands have been marked by Roman letters. They represent emission line ${}^5D_0 \rightarrow {}^7F_J$ transitions, where $J = 0, 1, 2, 3, 4$. The emergence of new peaks is shown by arrows.

D. High-pressure photoluminescence studies

In the next step, we attempted to map the local coordination changes around Eu^{3+} . $Y_{1.8}Eu_{0.2}Ge_2O_7$ shows photoluminescence behavior due to presence of Eu^{3+} ions in its lattice, as it is well known that emission lines splitting and their relative intensity can be used to probe point group symmetry and sometimes coordination polyhedron around Eu^{3+} ions [73].

PL spectra at ambient is shown in the Fig. 16(a). The characteristic emission from the interconfigurational $4f^n - 4f^{n-1}5d$ transitions of Eu^{3+} is seen [74–76]. These spectra result from the ${}^5D_0 \rightarrow {}^7F_J$ transitions, where $J = 0, 1, 2, 3, 4$. Because Eu^{3+} belongs to triclinic symmetry class (C_1) in the crystal system, the maximum number of stark splitting ($2J + 1$) is observed in the PL spectra. ${}^5D_0 \rightarrow {}^7F_1$ is magnetic dipole in nature and allowed by the Laporte selection rule. It is called magnetic dipole transition (MDT). The intensity of this line is not influenced by the external environment around Eu^{3+} ion and it is intense when crystal has center of symmetry [77]. The most intense transition observed in the PL measurement is from ${}^5D_0 \rightarrow {}^7F_2$. This is called hypersensitive induced electric dipole transition (EDT) and is strongly influenced by the local environment around Eu^{3+} ion. The higher the intensity of this peak, the lower is the symmetry around Eu^{3+} . ${}^5D_0 \rightarrow {}^7F_4$ transition is also electric dipole in nature and having remarkable intensity due to (C_1) site symmetry of Eu^{3+} ion. All these transitions are allowed by the standard Judd-Ofelt theory. However, in addition to these transitions, we also observe ${}^5D_0 \rightarrow {}^7F_0$ and ${}^5D_0 \rightarrow {}^7F_3$ transitions which are not allowed by the spectroscopic selection rules. This can be explained by the J -mixing of wave functions of same symmetry due to the presence of crystal field [78].

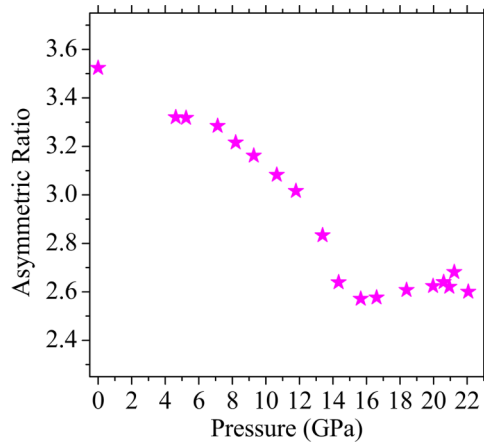


FIG. 17. The asymmetric ratio is plotted against the pressure. It is defined as the ratio of the integrated intensity of EDT to that of MDT.

The evolution of luminescence peaks with pressure is shown in Fig. 16. With increasing pressure, the spectra are seen to slightly shift toward higher wavelength. At low pressure luminescence peaks show broadening due to internal heterogeneous stress developed in the sample. Further increase in the pressure broadening remains constant till 10.5 GPa which is the hydrostatic limit of the PTM. Beyond this limit, the FWHM of the peaks increases due to quasi-hydrostatic stress environment. When the pressure is further increased to ~ 13.4 GPa, two new peaks, namely ($p1$) at ~ 579.1 nm and peak ($p2$) at ~ 585.3 nm gradually emerge. The appearance of these new peaks suggest that the symmetry around Eu^{3+} is changing and this is clear indication of the pressure induced structural phase transformation at pressure ~ 13.4 GPa, further supporting results from other studies. Peak ($p1$), can be assigned to corresponding ${}^5D_0 \rightarrow {}^7F_0$ transition in the new phase and hence the system has two distinct site symmetries for Eu^{3+} ions [79]. Similarly ($p2$) can be assigned to ${}^5D_0 \rightarrow {}^7F_1$ emission line in the new phase. Peak ($p2$) is also related to the symmetry changes around Eu^{3+} . To understand the evolution of symmetry around Eu^{3+} , a term called asymmetric ratio is defined as the ratio of integrated intensity of EDT to that of integrated intensity of MDT. The asymmetric ratio has been plotted in Fig. 17. The graph suggests that asymmetric ratio gradually decreases indicating Eu^{3+} acquires higher symmetry.

When pressure is increased to 18.4 GPa, there are new peaks emerging in bands III (EDT), IV, and V as well, which is clearly evident in their respective intensity profile modulation. The intensity of the new emerging peaks systematically increases with pressure because of the increasing fraction of the new phase of the compound. When pressure is increased

beyond 25.8 GPa, all the peaks show a tendency to shift towards higher wavelength except the new peak ($p2$), which shows a negative pressure gradient. It should also be noted that the number of new emission lines appearing in any of the bands is expected to be lower compared to the ambient phase because the asymmetric ratio clearly shows a transition to a higher symmetry coordination environment in the high-pressure phase. The highest pressure achieved in this experiment is ~ 45 GPa, and at this pressure a few emission lines of the ambient phase are still visible, which shows that the ambient polyhedral environment around Eu still exists at ~ 45 GPa. The new peaks, $p1$ and $p2$, remain visible upon complete pressure release, which shows that local structural changes are irreversible. From XRD and Raman measurements, it has been shown that long-range ordering has been completely lost upon pressure release, hence the changes in the local structure environment around the Eu^{3+} ion with pressure cycling are the same in the high-pressure crystalline phase as well as the amorphous phase.

V. CONCLUSION

Based on x-ray diffraction, XAS, Raman spectroscopic, and photoluminescence studies, we have reported irreversible pressure-induced amorphization with partial structural transformation to a distorted pyrochlore-type structure in $\text{Y}_{1.8}\text{Eu}_{0.2}\text{Ge}_2\text{O}_7$ at ~ 14.0 GPa under ambient temperature high-pressure studies. *In situ* laser heating the system at 13.1 GPa leads to the formation of an ordered pyrochlore structure. With a volume discontinuity of about 14% across the phase transition, it can be inferred that this transformation is first-order in nature. High-pressure XAS measurements around Y and Ge atoms suggest an increase in coordination number from seven to eight at Y sites, while four to six at Ge sites. Both the amorphous and the HP crystalline phases exhibit similar coordination around cations. HP photoluminescence studies suggest the existence of two different site symmetries for an Eu^{3+} ion that is sitting at a Y^{3+} site, and the HP phase has a more symmetric ligand environment around Eu^{3+} . The polymorphism reported here viz. a distorted pyrochlore, ordered pyrochlore, amorphous, and tetragonal phase in $\text{Y}_{1.8}\text{Eu}_{0.2}\text{Ge}_2\text{O}_7$ is expected to exhibit novel magnetic behavior and may be further explored from this point of view.

ACKNOWLEDGMENTS

The authors would like to acknowledge Dr. Velaga Srihari for user support at ECXRD beamline-11, Indus-2, and Dr. Nishant N. Patel for facilitating HP-HT studies. We are also thankful to Dr. T. Sakuntala for her continuous support. A.T. and S.N. thank Dr. A. K. Tyagi, Director, Chemistry Group, BARC for his constant encouragement in the research work.

- [1] E. Morosan, J. A. Fleitman, Q. Huang, J. W. Lynn, Y. Chen, X. Ke, M. L. Dahlberg, P. Schiffer, C. R. Craley, and R. J. Cava, Structure and magnetic properties of the $\text{Ho}_2\text{Ge}_2\text{O}_7$ pyrogermanate, *Phys. Rev. B* **77**, 224423 (2008).
 [2] K. M. Taddei, L. Sanjeewa, J. W. Kolis, A. S. Sefat, C. de la Cruz, and D. M. Pajerowski, Local-Ising-type magnetic order

and metamagnetism in the rare-earth pyrogermanate $\text{Er}_2\text{Ge}_2\text{O}_7$, *Phys. Rev. Mater.* **3**, 014405 (2019).

- [3] X. Ke, M. L. Dahlberg, E. Morosan, J. A. Fleitman, R. J. Cava, and P. Schiffer, Magnetothermodynamics of the Ising antiferromagnet $\text{Dy}_2\text{Ge}_2\text{O}_7$, *Phys. Rev. B* **78**, 104411 (2008).

- isotopic species of Mg_2SiO_4 , [Spectrochim. Acta Pt. A](#) **29**, 1007 (1973).
- [71] M. Gabelica-Robert, Contribution of vibrational spectroscopy to the study of the structure of pyro compounds, [J. Mol. Struct.](#) **79**, 255 (1982).
- [72] M. Maćzka, M. L. Sanjuán, A. F. Fuentes, L. Macalik, J. Hanuza, K. Matsuhira, and Z. Hiroi, Temperature-dependent studies of the geometrically frustrated pyrochlores $\text{Ho}_2\text{Ti}_2\text{O}_7$ and $\text{Dy}_2\text{Ti}_2\text{O}_7$, [Phys. Rev. B](#) **79**, 214437 (2009).
- [73] Y. Zhao, K. Chen, N. Li, S. Ma, Y. Wang, Q. Kong, F. Baudelet, X. Wang, and W. Yang, Tricolor Ho^{3+} photoluminescence enhancement from site symmetry breakdown in pyrochlore $\text{Ho}_2\text{Sn}_2\text{O}_7$ after pressure treatment, [Phys. Rev. Lett.](#) **125**, 245701 (2020).
- [74] J. H. V. Vleck, The puzzle of rare-Earth spectra in solids, [J. Phys. Chem.](#) **41**, 67 (1937).
- [75] B. R. Judd, Optical absorption intensities of rare-Earth ions, [Phys. Rev.](#) **127**, 750 (1962).
- [76] G. S. Ofelt, Intensities of crystal spectra of rare-Earth ions, [J. Chem. Phys.](#) **37**, 511 (1962).
- [77] C. Görrler-Walrand, L. Fluyt, A. Ceulemans, and W. T. Carnall, Magnetic dipole transitions as standards for Judd–Ofelt parametrization in lanthanide spectra, [J. Chem. Phys.](#) **95**, 3099 (1991).
- [78] J. E. Lowther, Spectroscopic transition probabilities of rare earth ions, [J. Phys. C](#) **7**, 4393 (1974).
- [79] K. Binnemans, Interpretation of europium(III) spectra, [Coord. Chem. Rev.](#) **295**, 1 (2015).